Glass Europe Vol. 2 (2024) 27-44
https://doi.org/10.52825/glass-europe.v2i.1382

Submitted: 18 Jun. 2024 | Accepted: 08 Jul. 2024 | Published: 23 Jul. 2024

# Mechanical and Electrochemical Properties of Lithium Aluminoborate Glasses

Theany To[1,*], Ismail Ladjani[1], Patrick Houizot[1], David Le Coq[2], Laurent Calvez[2], Alain Moreac[1], Sonia Braiek[1], Mickaël Le Fur[1], and Tanguy Rouxel[1,3]

[1] Univ Rennes, CNRS, IPR (Institut de Physique de Rennes) - UMR 6251, F-35000 Rennes, France

[2] Univ Rennes, CNRS, ISCR (Institut des Sciences Chimiques de Rennes) – UMR 6226, Rennes 35042, France

[3] Institut Université de France (IUF)

*Correspondence: Theany To, theany.to@univ-rennes.fr; theany.to@gmail.com

**Abstract.** The elastic moduli and the indentation behavior of glasses from the $x$$Li_2O$-5$Al_2O_3$-(95−$x$)$B_2O_3$ system, with $x$ = 35, 40, and 50 were characterized. Glasses become softer and less resistant to indentation cracking as the lithium content is increased, as a result of increasing the numbers of 3-fold coordinated boron and non-bridging oxygen atoms in this composition range. In parallel, the ionic conductivity at 25 °C is increased from 3.7 $10^{-10}$ to 5.5 $10^{-8}$ S·cm$^{-1}$, and the activation energy, as measured in the 10 to 90 °C ranges is between 55 (50 % $Li_2O$) and 65 (35 % $Li_2O$) kJ·mol$^{-1}$, which shows that the ionic diffusion of lithium is easier in Li-rich compositions. Measurements of the conductivity under a compressive load aligned with the electric field revealed a mechanical-electrical coupling. The change of the activation energy with the stress is associated with an activation volume, and thus a stress sensitivity, that is increased with the lithium content.

**Keywords:** Glass, Electrolyte, All-Solid-State Battery, Mechanics, Electrochemistry

## 1. Introduction

In an all-solid-state (ASS) battery, the electrolyte is a solid that, mostly, works also as a separator between the two electrodes, making the cell lighter and smaller compared to the conventional (Li-ions) one [1]. Advantages of ASS battery also include a low self-discharge, a large specific energy, and a more stable output voltage. However, the ionic conductivity of such electrolytes at ambient temperatures must be enhanced and the manufacturing cost must be reduced while improving the performance. The formation and propagation of lithium dendrites must be prevented, the volume changes during electrochemical cycling must be accommodated, and the cell must resist internal and external forces during battery assembling or/and stacking [2], [3], [4], [5]. In order to achieve this objective, the mechanical properties as well as the pressure dependence of the electromechanical properties of ionic conductive materials need to be investigated [2].

Glassy electrolytes offer an interesting alternative to the currently developed crystallized ones [6], [7], [8]. Glasses possess a viscoelastic forming ability resulting in more stable electrolyte/electrode interface with a better bonding. Moreover, the disordered atomic structure of glass hinders the formation of lithium dendrites and allows great flexibility in composition within a chemical system, which allows to tune and enhance the electrochemical and mechanical properties. However, compared to crystallized electrolytes, glassy ones exhibit a smaller ionic conductivity, which remains typically below $10^{-4}$ S·cm$^{-1}$ at ambient temperature. Nevertheless,

glass can be transformed into glass-ceramics by heat-treatment above the glass transition temperature ($T_g$) and, most often, a significant enhancement of the conductivity is observed [9]. Although there are known issues regarding the mechanical properties and the effect of the stress field on the ionic conductivity, the mechanical properties of ionic conductive glasses were little studied so far. The cracking behavior of glassy electrode materials in lithium batteries, and the fracture toughness of glassy oxide electrolytes are reported in Refs [10] and [11], respectively. The viscoplastic behavior and indentation resistance of glassy sulfide electrolytes is reported in [12], [13].

Among ionic conductive glasses, alkali borates, and in particular Li-borate, have been widely studied, although their ionic conductivity is lower than that of chalcogenide glasses [14], [15], [16]. This is because the atomic structure of Li-borate glasses is quite well-known and is very sensitive to the composition change, so that the glasses from such chemical systems offer an opportunity to investigate the role of the atomic network structure on the ionic conductivity. The ionic conductivity of lithium borate glasses was studied in the 50-500 °C temperature ($T$) range and follows an Arrhenius dependence on $T$ resulting in a conductivity of $10^{-23}$ and $10^{-7}$ S·cm$^{-1}$ at $T$ ~ 20-25 °C for 10 and 50 mol% of lithium oxide, respectively [14], [15], [16]. The mechanical properties and mechano-electrochemical couplings were rarely studied though, likely because of their hygroscopic behavior and because only thin and small specimens are mostly available.

The present study deals with the mechanical and electrochemical properties of glassy electrolytes from the lithium aluminoborate system, as well as the effect of a mechanical loading on the ionic conductivity. Aluminoborate were preferred over borate glasses as the addition of alumina allows to limit the sensitivity to moisture. Three glasses were considered with changing the Li content, and cm$^3$ size homogeneous samples were obtained. Their density, elastic moduli, hardness, and crack resistance were characterized, and their structure was studied in the light of Raman spectra and taking advantage of published data on similar glasses [17], [18]. The ionic conductivity ($\sigma_i$) was measured from 10 to 90 °C by means of impedance spectroscopy using *AC* current. The effect of a mechanical loading on $\sigma_i$ was investigated by means of a home-made dead-weight testing machine. Finally, the intercorrelation between the mechanical and electrical behavior is discussed in the light of the glass structure.

# 2. Experimental Procedures

## 2.1 Sample preparation

Three glasses, $x$Li$_2$O-5Al$_2$O$_3$-(95−$x$)B$_2$O$_3$, with $x$ = 35, 40, and 50 mol.%, were synthesized by the melt-quenching-annealing method. These glasses are referred to as 35LiAlB, 40LiAlB, and 50LiAlB. Lithium carbonate (Li$_2$CO$_3$, > 98%, Merk KGaA), alumina (Al$_2$O$_3$, > 98%, Merk KGaA), and boric acid (H$_3$BO$_3$, > 99%, Honeywell International) were used as raw materials. Powders were dry mixed and homogenized prior to melting in a Pt-Rh crucible between 840 and 900 °C, depending on the composition, for 1.5 h. The melt was then poured and quenched into a pre-heated super-alloy (Inconel 600) mold. The mold was preheated at a temperature between 330 to 410 °C depending on the composition so as to reduce the thermal shock amplitude. After this preliminary treatment for 1 h, samples were further annealed at $T_g$, as measured by differential scanning calorimetry (DSC), for 30 min. Testing specimens were then cut to the desired shape and polished down to a 1 µm (water-free) diamond paste.

## 2.2 Glass transition temperature

The glass transition temperature ($T_g$) was measured by means of DSC (Netzsch, Selb, Germany). A bulk glass sample having a disk-like shape with a diameter of 5 mm was polished to have a total weight of around 45 mg. The glass sample was then placed in a Pt crucible and heated up to 420-500 °C (depending on the glass composition) at a heating/cooling rate of 10

°C·min$^{-1}$ under a $N_2$ gas flow of 10 mL·min$^{-1}$. Finally, $T_g$ was determined from the intercept between the extrapolated sub-$T_g$ signal and the tangent of the endothermic shift observed in transition range.

## 2.3 Raman spectroscopy

Raman spectra were acquired using a micro-Raman spectrometer (HR-Evo, Horiba Scientific). A 532 nm green diode laser was used to excite the sample surface for an acquisition time of 10 s. No heating effect has been observed. The spectral range extended from 0 to 1700 cm$^{-1}$ with a 1.7 cm$^{-1}$·px$^{-1}$ dispersion which correspond to a spectral resolution around 5 cm$^{-1}$. At least two spectra from two different locations on the glass were recorded for each specimen.

## 2.4 Density, atomic packing, and molar volume

The density ($\rho$) of the glass was measured by means of Archimedes' principle in pure ethanol (> 99.99%) at room temperature (22 °C). The density was further used to estimate the atomic packing density ($C_g$), the molar volume of a gram-atom of glass ($V_0$), and the molar volume of glass associated with one Li atom ($V_{Li}$) as,

$$C_g = \frac{N_A \sum_i (4/3)\pi x_i r_i^3}{V_0} \quad (1)$$

$$V_0 = \frac{\sum_i x_i m_i}{\rho} \quad (2)$$

$$V_{Li} = \frac{V_0}{x_{Li}} \quad (3)$$

where $N_A$ is the Avogadro number. $x_i$, $r_i$, and $m_i$ are the atomic fraction, ionic radius, and the molar mass of the i$^{th}$ element of a glass, where $\Sigma_i\, x_i = 1$. $x_{Li}$ is the atomic fraction of Li. The ionic radius is taken from Ref. [19]. The ionic radii of Li, Al, B, and O are 0.59, 0.39, 0.11, and 1.35 Å, respectively.

## 2.5 Ultrasonic echography and indentation

Cut and polished glass parallelepipedal samples, 15×25×6 mm$^3$, were used to determine the elastic moduli, and further the hardness ($H$) and the crack resistance ($CR$). Elastic moduli at room temperature (25 °C) were obtained using ultrasonic echography (USE) by means of 10 MHz piezoelectric transducers in contact with the sample via a coupling gel. Young's modulus ($E$) and shear modulus ($G$) are derived from the acoustic wave velocity and from the glass density according to Eqs. 4 and 5 as [20],

$$E = \rho \frac{3V_L^2 - 4V_T^2}{\left(\frac{V_L}{V_T}\right)^2 - 1} \quad (4)$$

$$G = \rho V_T^2 \quad (5)$$

where $V_L$ and $V_T$ are the longitudinal and transversal wave velocities, respectively. Then Poisson's ratio ($\nu$) and the bulk modulus ($K$) can be calculated,

$$\nu = \frac{E}{2G} - 1 \quad (6)$$

$$K = \frac{E}{3(1-2\nu)} \quad (7)$$

Vickers indentation (Matsuzawa VMT-7S) at ambient atmosphere (i.e., at room temperature of 25 °C and relative humidity of 45 %) was used to determine hardness (*H*) and the crack initiation resistance (*CR*). We performed a sequence of indentation tests by using a stepwise increasing load ($P_i$) from 0.3 to 4.9 N. The loading/unloading duration and dwell time were set at 15 s. Twenty indents were made on each glass sample and for each load. In order to identify the possible indentation size effect, hardness was averaged over 20 imprints for each load. *H* represents a normal contact stress and is expressed as the ratio of the load on the projected imprint area as [21],

$$H = \frac{2P_i}{d^2} \tag{8}$$

where *d* is the average over the two diagonal lengths of an indent. Note that *H* is given in Pa and differs from the Vickers hardness number (HV). The crack initiation resistance is the indentation load at which 50 % crack probability is recorded [22]. For a Vickers indenter, the crack probability is 100 %, 75 %, 50 %, 25 %, and 0 % when there are four, three, two, one, and zero (radial/median type) corner cracks, respectively.

## 2.6 Ionic conductivity measurement

The ionic conductivity ($\sigma_i$) was measured as a function of temperature and pressure. For the temperature dependence, the measurement was conducted by means of an Autolab workstation (PSTAT302N with FRA32 M and ECD module) in the 25 to 90 °C temperature range. The frequency (*f*) varied from 1 MHz to 1 Hz, with a signal amplitude of 100 mV. Measurements were performed on 10 mm in diameter and 1.5 mm thick polished (down to 1 μm) disks (pellets). Pellets were coated with Au thin layers on both mirror-polished sides prior to the measurements, using a low vacuum coater (EM ACE200, Leica Microsystems). The pressure dependence of the ionic conductivity was investigated by means of a home-made testing machine consisting of dead load mechanism similar to that of a creep machine, which allows to apply a uniaxial compression on a 10 mm diameter disk of glass, and an ionic conductivity cell equipped with a heating plate (above described Autolab workstation) (Figure 1).

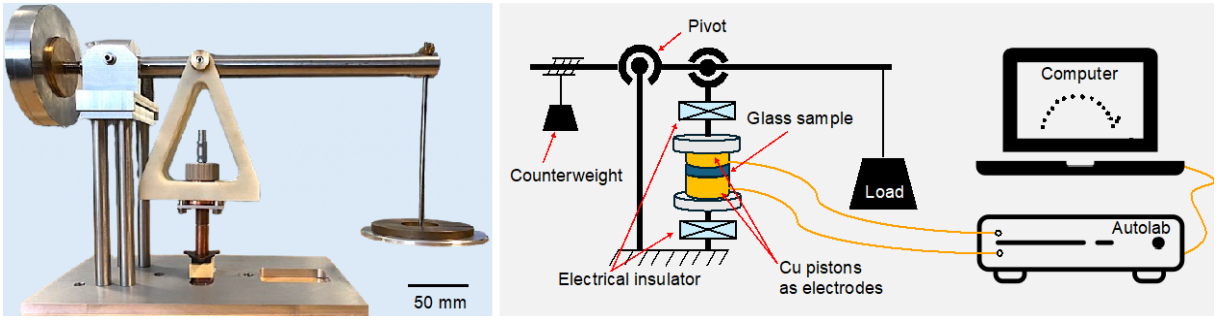


***Figure 1**. Photograph of the device operating inside a glove box (left); kinematic chain of the loading device (right).*

After each experiment, the Nyquist diagram is analyzed by fitting a reasonable model in order to determine the real ionic resistance of the glass ($R_g$). In this study, a constant phase element (CPE) is used to replace the ideal capacitor [23]. The complex impedance of a CPE circuit is expressed as,

$$Z_{CPE} = \frac{1}{Y_0(i\omega)^n} \tag{9}$$

where $\omega$ is the angular frequency ($\omega = 2\pi f$), and $Y_0$ and *n* are the characteristic parameters of the CPE. The complex impedance of the parallel circuit ($Z_p$) between a CPE and the ionic glass resistor ($R_g$), denoted $R_g$ //CPE can then be expressed as,

$$Z_p = \frac{R_g}{1+(i\omega)^n Y_0 R_g} \quad (10)$$

In this study, the resistance of the system ($R_s$) is not negligeable and increases with increasing temperature. Moreover, there is always a tail on the low frequency side of each depressed semicircle, which is known to contribute to the polarization due to the accumulation of ions in-between the electrodes and the electrolyte. The addition of $R_s$ and a CPE (for the polarization tail) in series to $Z_p$ results in the following expression for the complex impedance of the circuit,

$$Z = R_s + \frac{R_g}{1+(i\omega)^{n_1} Y_{01} R_g} + \frac{1}{Y_{02}(i\omega)^{n_2}} \quad (11)$$

where $Y_{01}$ and $n_1$ are the characteristic parameters of the CPE in the $R_g$//CPE circuit, and $Y_{02}$ and $n_2$ are those of the CPE in series circuit. Finally, the ionic conductivity was calculated from the equation below:

$$\sigma_i = \frac{t}{R_g \times A} \quad (12)$$

where $t$ and $A$ are the thickness and the cross-section area of the specimen. It should be noted that the overall conductivity, $\sigma = \sigma_i + \sigma_e$, is measured, but in the present case, the electronic conductivity, $\sigma_e$, is negligible.

# 3. Results and Discussions

## 3.1 Glass structure

The Raman spectra of the three glasses exhibit the known features of alkali borate glasses, with additional bands from structural units related to the addition of $Al_2O_3$ (Figure 2). The peaks at 90 $cm^{-1}$ for the 35LiAlB and 40LiAlB, and at 95 $cm^{-1}$ for 50LiAlB corresponds to the so-called “boson” peak [24], [25]. This low wave-number range of excess vibrational density of states originates from quasi-localized vibrations of string-like dynamical defects [24], likely over-coordinated structural units [25]. This peak, which cannot be unambiguously attributed, will not be discussed in this paper as this would go far beyond the scope of this paper.

For alkali aluminoborate glasses, the band between 380 and 650 $cm^{-1}$ attributed to B-O-B, Al-O-Al, and B-O-Al stretching in $B^{IV}$ and $Al^{IV}$ units [26], [27]. The peaks at 505 and 550 $cm^{-1}$ are attributed to superstructural groups like the diborate units ($B_4O_9$). The peak at ~ 450 $cm^{-1}$ was not previously reported in alkali borate glasses [16] and would hence stem from the incorporation of aluminum, presumably $Al^{IV}$ in the present case since it does not depend on the lithium oxide content nor on the boron oxide content. The most prominent change in the spectra as the Li content is increased is the decrease of the peak at ~ 770 $cm^{-1}$ (765 $cm^{-1}$ for 50LiAlB), and the increase of the peaks at 835, 950-970, 1250, and 1480 $cm^{-1}$. It is well known that the addition of $Li_2O$ into a borate glass transforms the boroxol rings (rings with three neutral $BO_3$ units, generally associated with a peak at ~ 808 $cm^{-1}$ for glass with relative low alkali oxide) into rings with two $BO_4$ and one neutral $BO_3$ unit [28]. The shifts of the Raman peak to ~ 770 $cm^{-1}$ (for 35LiAlB and 40LiAlB) and ~ 765 $cm^{-1}$ (for 50LiAlB) reflect this transformation. Therefore, the decrease in intensity of these peaks from 35LiAlB to 50LiAlB is due to the disappearance of $BO_3$ units to the benefit of the rings with two $BO_4$ and one neutral $BO_3$ unit. The transformation of the mentioned rings comes along with the increase of the superstructural units like the orthoborate, mixed Al-B structure, and diborate groups as seen in the peak at 950-970 $cm^{-1}$ [29], [30], [31], and the fast development of a charged borate triangle (the pyroborate unit $B_2O_5^{4-}$ with 2 non-bridging oxygens (NBO) per boron) as seen in the peaks at 835 and 1250 $cm^{-1}$ [29], [30]. The peak at around 870 $cm^{-1}$ is not observed in the binary alkali borate glasses, and is likely to relate to the tetrahedral $AlO_4$ group, which is found in alkali

galloborate glasses when the $B_2O_3$ content is less than 50 mol% [32], [33]. Also, the increase of the peak at ~ 1480 $cm^{-1}$ for the glass with larger lithium oxide content is due to the formation of metaborate triangles, which possess 2 bridging oxygens (BO) and one NBO, $BO_{2/2}O^-$ [29], [34], [35]. In general, the formation of triangular metaborate and pyroborate units results in an increase in the numbers of NBOs per boron.

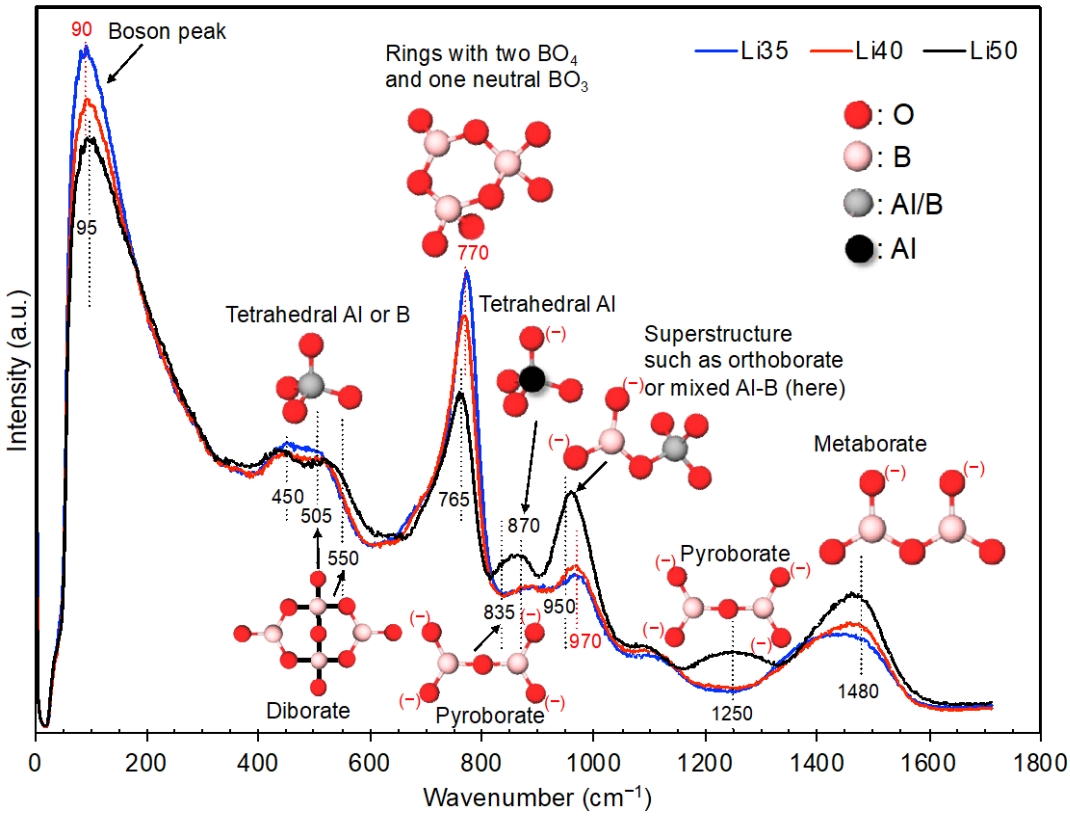


***Figure 2**. Raman spectra recorded for the three studied glasses (i.e., 35LiAlB, 40LiAlB, and 50LiAlB). The red, purple, grey, and black balls represent the O, B, Al/B, and Al atoms, respectively. NBOs are indicated by (−) sign next to the O atoms.*

The glass structure models and NMR experiments from literature [17], [18] corroborate the Raman results. Since the lithium aluminoborate (LiAlB) glasses in this study have low alumina content (5 mol%), their structures should not differ much from those of lithium borate (LiB) glasses. Figure 3 shows the concentration of four-fold coordinated boron species ($BO_4$) and of non-bridging oxygen (NBO) in LiB [14] and LiAlB [18] glasses. For the binary lithium borate glasses, the concentration of $BO_4$ and NBO can be estimated as a function of the $[Li_2O]/[B_2O_3]$ ratio following a procedure detailed in Refs. [17], [18], and was found in agreement with the NMR results. This estimation leads to three regions of interest. For the $[Li_2O]/[B_2O_3]$ ratio from 0 to 0.4 (0 to 30 mol% of $Li_2O$, and four-fold coordination boron $N_4$ = $[Li_2O]/[B_2O_3]$), all the O from the addition of $Li_2O$ joins the glass-forming network, resulting in increasing of $BO_4$ without creating any NBOs, as revealed by the sharp increase of $BO_4$ species in Figure 3. For the $[Li_2O]/[B_2O_3]$ ratio between 0.4 and 0.7 (between 30 mol% and 40 mol% of $Li_2O$, $N_4$ = 1/3 + (1/6) $[Li_2O]/[B_2O_3]$), the addition of each $Li_2O$ creates two NBOs, and reduces the rate of formation of $BO_4$ units. For $[Li_2O]/[B_2O_3]$ ratio between 0.7 and 1 (40 to 50 mol% of $Li_2O$), $N_4$ = 5/8 + (1/4) $[Li_2O]/[B_2O_3]$, and the content in $BO_4$ units starts to decrease since the excess $Li_2O$ favors the formation of NBOs, as seen in the steep increasing of the NBO line (red dashed line and crossed point) in Figure 3.

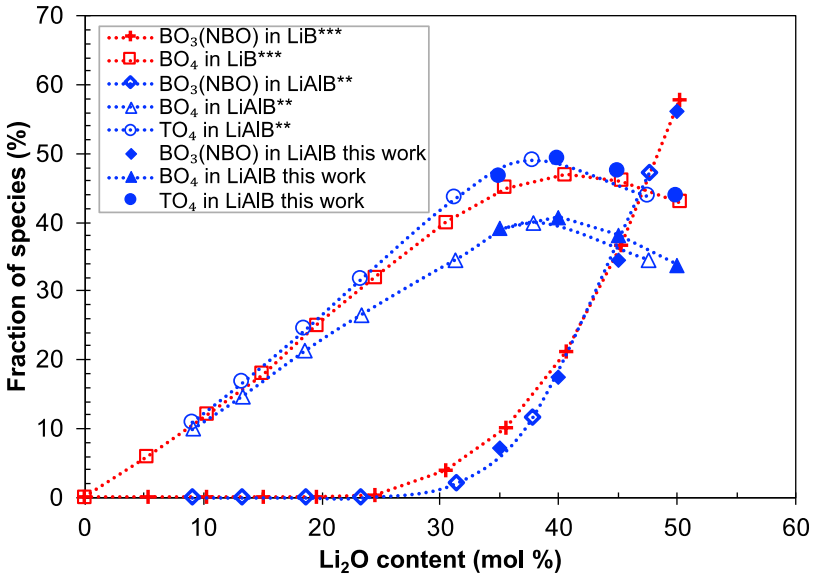


***Figure 3**. Structural unit speciation in lithium borate (LiB) and lithium aluminoborate (LiAlB) glasses. Red and blue colors represent LiB and LiAlB series, respectively. The dashed lines are guidelines for the eyes. NBO means non-bridging oxygen, and $TO_4$ means $BO_4$ + $AlO_4$. ***Data from Ref. [14]. **Data from Ref. [18]. Solid marks are from this study.*

The same explanation holds for lithium aluminoborate glasses. In Figure 3, $BO_4$ units are distinguished from the overall four-fold coordinated units ($TO_4$), which is the sum of $BO_4$ and $AlO_4$ (four-fold coordinated aluminum) units. Both $TO_4$ (round points in Figure 3) and $BO_4$ (triangle points in Figure 3) amounts increase linearly as the $Li_2O$ content is raised from 10 to 30 mol%. The rate of increase slows down above 30 mol% $Li_2O$ until the content in tetrahedral units reaches a maximum at about 40 mol% $Li_2O$, which is related to the occurrence of three-fold coordinated boron with non-bridging oxygen (noted as $BO_3$(NBO), rhombus point in Figure 3) [14]. Above 40 mol% of $Li_2O$, the $BO_3$(NBO) content increases steeply resulting in the decreases of the $TO_4$ and $BO_4$ contents. The change in the difference between the $TO_4$ and the $BO_4$ contents suggests an increase of the $AlO_4$ concentration above 20 mol% $Li_2O$ [18]. As seen in Figure 3, the presently studied glasses are in the composition range where the fractions of 4-fold coordinated units (Al or B-centered) change little with the Li content. This interpretation of the glass structures will be used in the next section to discuss the mechanical and electrical properties.

## 3.2 Glass transition temperature, atomic packing characteristics and elastic properties

***Table 1**. Glass transition temperature ($T_g$), density ($\rho$), Young's modulus (E), shear modulus (G), Poisson's ratio ($\nu$), bulk modulus (K), atomic packing density ($C_g$), molar volume (gram-atom) of glass ($V_0$), and molar volume (gram-atom) of glass per Li ion ($V_{Li}$) of $35Li_2O$-$5Al_2O_3$-$60B_2O_3$ (35LiAlB), $40Li_2O$-$5Al_2O_3$-$55B_2O_3$ (40LiAlB), $50Li_2O$-$5Al_2O_3$-$45B_2O_3$ (50LiAlB). The maximum error values are given in brackets.*

| Glass ref. | $T_g$ [°C] (5) | $\rho$ [g·cm$^{-1}$] (0.005) | $E$ [GPa] (2) | $G$ [GPa] (2) | $\nu$ (0.005) | $K$ [GPa] (2) | $C_g$ (0.005) | $V_0$ [cm$^3$·mol$^{-1}$] (0.02) | $V_{Li}$ [cm$^3$·mol$^{-1}$] (0.02) |
|---|---|---|---|---|---|---|---|---|---|
| 35LiAlB | 464 | 2.284 | 83 | 33 | 0.261 | 58 | 0.584 | 5.84 | 35.86 |
| 40LiAlB | 431 | 2.293 | 84 | 34 | 0.253 | 57 | 0.584 | 5.75 | 30.17 |
| 50LiAlB | 378 | 2.253 | 79 | 31 | 0.277 | 59 | 0.568 | 5.70 | 22.28 |

$T_g$ temperatures, density, $C_g$, molar volumes, and elastic moduli are summarized in Table 1. $T_g$ decreases from 464 to 378 °C with increasing the $Li_2O$ content from 35 to 50 mol. %. As seen in Figure 4, $T_g$ of both LiB and LiAlB exhibits bell-shape curves with a maximum of

$T_g$ at 30 mol.% $Li_2O$. The maximum of $T_g$ is associated with the initial occurrence of $BO_3$(NBO) (see Figure 3 in § 3.1). The formation of $BO_3$(NBO) units results in a decrease of the network connectivity and dimensionality, and therefore in a decrease $E$ and $G$. Shear deformation becomes easier as the structure adopts an increasingly two-dimensional character, and therefore Poisson's ratio is increased. Besides, the formation of Li-O bonds at the NBO sites, which are weaker than the other interatomic bonds in the glass, and the decrease of $C_g$ at $Li_2O$ content larger than 40 mol.% lead to a decrease of $T_g$ (recall that $T_g$ follows the same trend as the molar dissociation energy [36]) which is corroborated by previously published data [36], [37]. The inversion point at 20 mol% of $Li_2O$ may be explained by the existence of $AlO_4$ units. For $Li_2O$ below 20 mol%, the overall amount of tetrahedrally coordinated boron and aluminum units ($TO_4$) in LiAlB is slightly greater than the amount of $BO_4$ units in LiB glasses (Figure 3). Therefore, the increase of the $Li_2O$ content results in an increase of the amount of $AlO_4$ units and induces a stiffening of the glass structure. As a result, LiAlB glasses have larger $T_g$ temperatures than LiB glasses (Figure 4a).

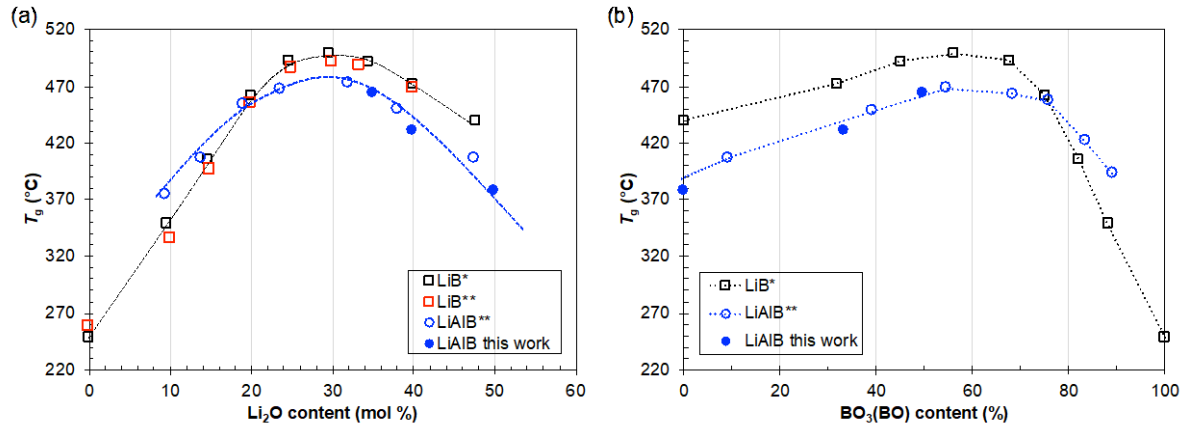


***Figure 4**. $T_g$ dependence on (a) the $Li_2O$ content and (b) the $BO_3$ triangle with bridging oxygens ($BO_3$(BO)), for lithium borate (LiB) and lithium aluminoborate (LiAlB) glasses. Black and blue dashed curves are guides for eyes. *Data extracted from Ref. [37]. **Data extracted from Ref. [18].*

For $Li_2O$ content above 20 mol%, the amount of $AlO_4$ units becomes large enough so that the overall amount of $TO_4$ groups significantly exceeds the amount of $BO_4$ groups in LiAlB glasses, although the $TO_4$ content in LiAlB is still greater than the $BO_4$ one in LiB (Figure 3). The replacement of the $BO_4$ units by the $AlO_4$ ones results in a decrease of the network energy because the Al-O bond energy (385 kJ $mol^{-1}$ for $Al^{IV}$) is smaller than the B-O one (525 and 394 kJ $mol^{-1}$ for $B^{III}$ and $B^{IV}$, respectively) [19]. Therefore, LiAlB glasses exhibit smaller $T_g$ values than LiB ones. However, in the case of the addition of $Li_2O$, the evolution of the structure toward a more tri-dimensional network thanks to the formation of $BO_4$ units [27], [28] predominates over the weakness of the Li-O bond (146 kJ $mol^{-1}$), so that a considerable increase in $T_g$ is observed for both LiB and LiAlB glasses (until the amount of $Li_2O$ reaches 30 mol%) [18]. Consistently, the decrease of $T_g$ of both glass series for $Li_2O$ content above 30 mol% is due to the increase of the $BO_3$(NBO) content.

The dependence of $T_g$ of LiB and LiAlB glasses on the concentration of the boron-oxygen triangles with bridging oxygen atoms is illustrated in Figure 4b. According to these data, the tetrahedral layered structure starts manifesting itself when the concentration of $BO_3$(BO) is around 75 mol%, i.e., when the $BO_3$(BO) content is three times larger than the $BO_4$ one in the LiB system or than the $TO_4$ one in LiAlB system. Again, this inversion point at 75 mol% of $BO_3$(BO) unit corroborates the one of the $Li_2O$ content at 20 mol% in (Figure 4a).

A slight increase of $\rho$, $E$, and $G$ is first observed as the $Li_2O$ content is increased from 35 to 40 mol. %. Followed by a decrease at larger lithium content. This trend can be explained by the fact that an increase of the $Li_2O$ content from 35 to 40 mol% in LiAlB glasses leads to an increase of the $TO_4$ content (Figure 3), which should result in an increase of the stiffness

and of the network connectivity [38]. However, this effect is counterbalanced by the concomitant increase of the $BO_3$(NBO). As a matter of fact, 35LiAlB and 40LiAlB glasses have very close properties (Table 1). At larger $Li_2O$ content, the amount of $TO_4$ decreases and the $BO_3$(NBO) content increases dramatically, which results in a decrease of $\rho$, $E$, and $G$ while $\nu$ is increased [38].

## 3.3 Indentation behavior

At loads below 5 N, $H$ decreases quite significantly as the load is increased whatever the $Li_2O$ content (Figure 5a). This is the so-called indentation size effect (ISE) [39], [40], [41]. $H$ reaches a plateau at a sufficient load (~5 N). Again, $H$ decreases with increasing $Li_2O$ content and the values of 5.4, 5.3, and 5.0 GPa are measured in the load-independent region for the 35LiAlB, 40LiAlB, and 50LiAlB glasses, respectively. This decrease can be explained by the change of the boron coordination from IV to III, which is associated with a decrease of the atomic network connectivity and of $C_g$ and an increase of free volume content (Table 1).

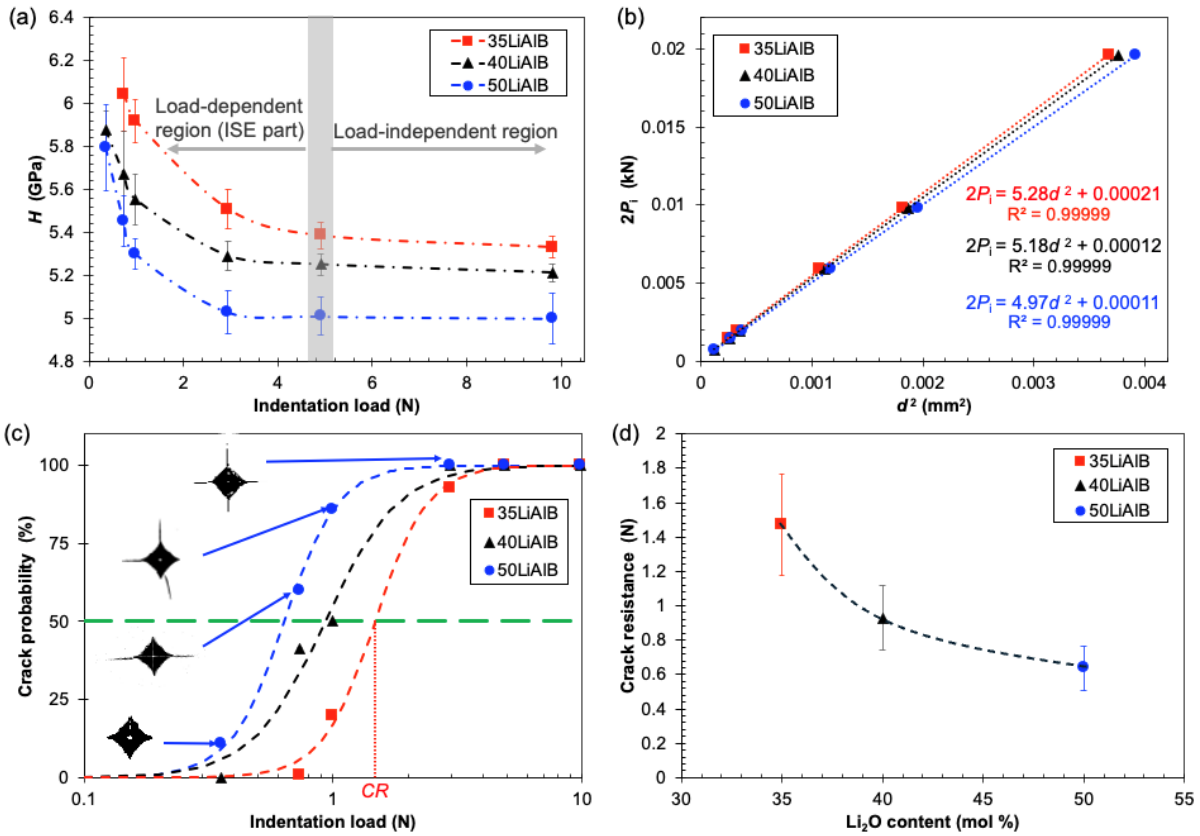


***Figure 5**. (a) The indentation size effect (ISE). The dashed lines are guides for the eyes; (b) Applied indentation load versus indentation diagonal length according to the Hays-Kendall model; (c) Indentation crack resistance curves. The four inset images show the most occurrent cracking behavior corresponding to an increasing load for the 50LiAlB; (d) Dependence of CR on the Li2O content. The dashed line is guide for the eyes.*

Several models were proposed to describe the ISE behavior [39], [40], [41]. Among these models, the one by Hays and Kendall [41] proposed that there exists a minimum indentation load $P_{min}$ (specimen resistance) necessary to initiate plastic deformation, and the approach provides a good estimation of the load-independent hardness ($H_{load\text{-}ind}$). According to this approach, the load-independent hardness is expressed as,

$$H_{load-ind} = \frac{2(P_i - P_{min})}{d^2} \quad (13)$$

From Eq. (13), a plot of $2P_i$ as a function of $d^2$ yield a straight line, from which $2P_{min}$ and $H_{load\text{-}ind}$ can be easily determined, (Figure 5b). As shown by the correlation coefficient ($R^2$), Eq. (13) provides a good description of the experimental data. $H_{load\text{-}ind}$ values of 5.28, 5.18, and 4.97 GPa were obtained this way for the 35LiAlB, 40LiAlB, and 50LiAlB glasses, respectively, corresponding to $P_{min}$ values of 0.1, 0.06, and 0.05 N.

The indentation cracking resistance is shown in Figure 5c. At the indentation load of 0.7 N, the 35LiAlB glass does not exhibit any corner crack (0 % crack probability), while the crack probability of the 40LiAlB and 50LiAlB glasses are close to 40 and 60 %, respectively. The crack resistance (*CR*) was estimated from the smooth fitting (sigmoidal shape) of the data point in Figure 5c. The decrease of *CR* with increasing $Li_2O$ content is chiefly attributed to the decrease of the mean network cohesive energy [19] due to the formation of Li-O bonds, which are likely to provide an easy path for the crack.

## 3.4 Ionic conductivity

### 3.4.1 Temperature dependence

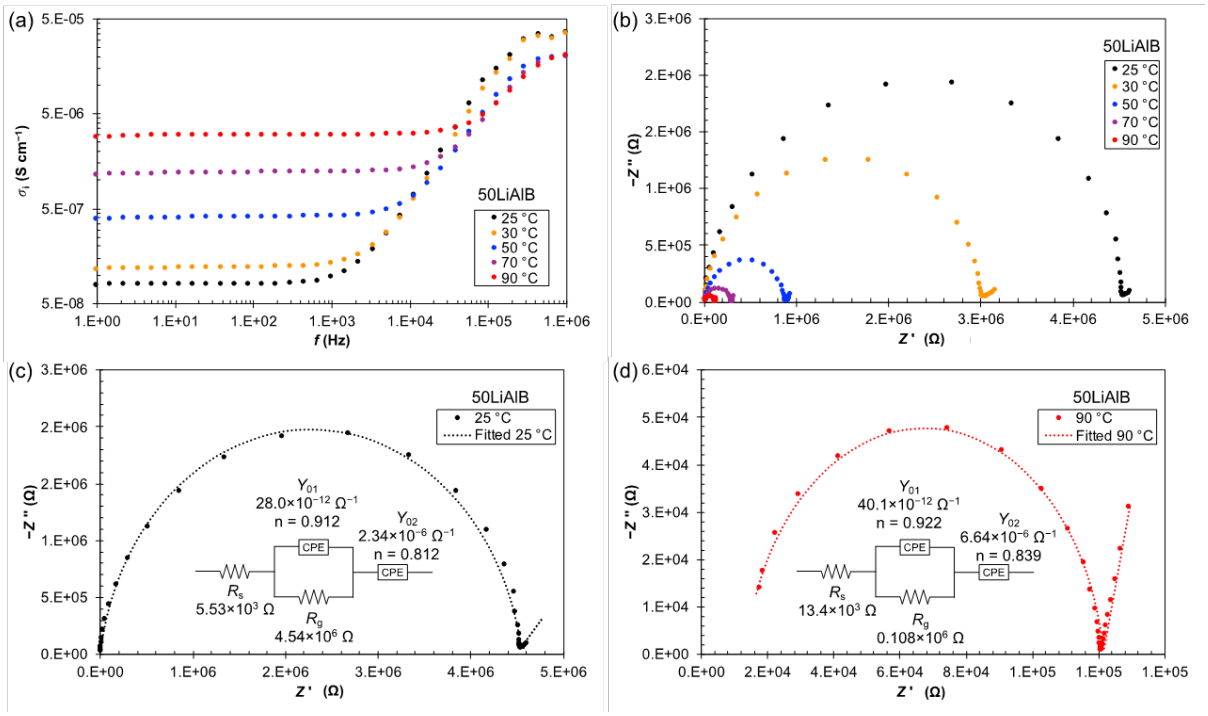


***Figure 6**. (a) Conductivity spectra ($\sigma'_i$) for the 50LiAlB at different temperatures. (b) Corresponding Nyquist plots. (c) Modelling of the data obtained with the 50LiAlB at 25 °C. (d) (c) Nyquist plot (red round point) and fitted curve (dotted line) for the 50LiAlB at 90 °C.*

The Nyquist diagrams for the 50LiAlB glass are shown in Figure 6b, for temperature between 25 °C and 90 °C, and for frequency ranging from 1 Hz to $10^6$ Hz. The radius of the depressed semicircle decreases with increasing temperature. Besides, the depressed semi-circles exhibit heights smaller than half of their diameters. Therefore, the simple classical parallel R//C circuit is not pertinent in the present case. A constant phase element (CPE) is used to replace the ideal capacitor [23]. The resistance of the system ($R_s$) is not negligeable and increases with increasing temperature. The experimented data points can be smoothly fitted by Eq. (11). In the present case, $n_1$ is close to 0.9 ± 0.03, and independent of composition and temperature. The ionic conductivity is calculated by means of Eq. (12) using the $R_g$ values obtained from the fit of Nyquist diagrams as in Figure 6c-d.

The ionic conductivity increases with increasing the $Li_2O$ content, and increases by about two orders of magnitude as the temperature is raised from 25 to 90 °C (Figure 7a). At room temperature (25 °C), the largest $\sigma_i$ value is of 7.96 × $10^{-8}$ S·$cm^{-1}$ (50LiAlB), while the 35LiAlB glass is the less conductive with $\sigma_i$ = 4.26 × $10^{-10}$ S·$cm^{-1}$. At 90 °C, the ionic conductivity of the 50LiAlB glass reaches 3.35 × $10^{-6}$ S·$cm^{-1}$. According to the Nernst-Einstein relationship [43], the diffusion coefficient is expressed as $D = \sigma_i (k\,T) / ([C]\,q^2)$, where $[C]$ is the charge carrier molar concentration, and q is the charge (q = +1 | $e^-$ |). Since the temperature dependence of the diffusion coefficient is given by $D = D_0 \exp[-\Delta G_a / (R\,T)]$, the temperature dependence of $\sigma_i$ is expressed as,

$$\sigma_i = \frac{\alpha_0}{T} e^{-\frac{\Delta G_a}{RT}} \tag{14}$$

where $\Delta G_a$ is the free activation enthalpy of the ionic conductivity, $\alpha_0$ is a pre-exponential factor, $T$ is the temperature in kelvins, and $R$ is the universal gas constant.

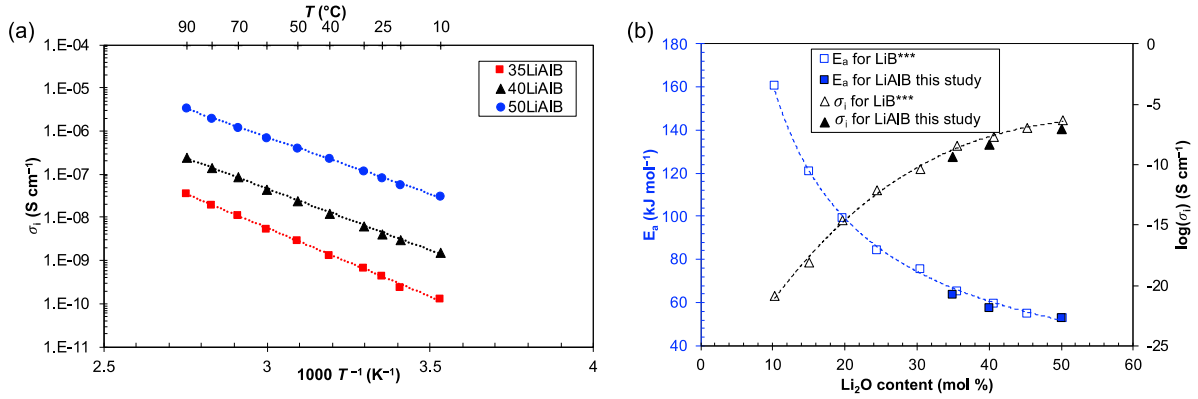


***Figure 7**. (a) Arrhenius diagram of the DC-conductivity. The dotted lines are obtained by fitting the experimental results with Eq. (14). (b) Changes of ($E_a$) and $\sigma_i$ with composition at room temperature (25 °C) (data on LiB glasses extrapolated from Ref. [14]). The dashed lines are guides for the eyes.*

As seen in Figure 7a, the experimental points follow a straight line indicating that the $T$-dependence of the ionic conductivity is in agreement with Eq. (14). The logarithmic form of Eq. (14) is expressed as,

$$\ln(T\sigma_i) = \ln(\alpha_0) - \frac{\Delta G_a}{RT}. \tag{15}$$

Taking the differential of Eq. (15) with respect to reversed temperature, one obtains:

$$-R\frac{\partial \ln(T\sigma_i)}{\partial(1/T)} = \Delta G_a + \frac{1}{T}\left(\frac{\partial \Delta G_a}{\partial(1/T)}\right). \tag{16}$$

Since, by definition, $-(\partial \Delta G_a / \partial T)$ is the activation entropy, $\Delta S_a$, Eq. (16) can be written as:

$$-R\frac{\partial \ln(T\sigma_i)}{\partial(1/T)} = \Delta G_a + T\Delta S_a\,, \tag{17}$$

and thus, recalling that $\Delta H_a = \Delta G_a + T\,\Delta S_a$, we obtain,

$$-R\frac{\partial \ln(T\sigma_i)}{\partial(1/T)} = \Delta H_a \tag{18}$$

This simple derivation shows that the experimentally available measure, the apparent activation energy $E_a$, is indeed the activation enthalpy of the diffusion process.

$\sigma_i$ at 25 °C and $E_a$ calculated from the Eq. (18) are plotted in Figure 7b, together with results of LiB glasses extrapolated from Ref. [14]. The present results are close to those obtained on aluminum-free lithium borate glasses. The ionic conductivity increases while the activation energy decreases, from $E_a$ ~ 64 to 50 kJ mol$^{-1}$, as the $Li_2O$ content is increased, which suggests that the incorporation of Li ions in the network makes the diffusion of Li ions easier.

The addition of $Li_2O$ into LiB glasses leads to a relatively large increase of the amount of $BO_4$ units for $Li_2O \leq 30$ mol%, and further to a smaller increase of this amount (together with an increase of the $BO_3$(NBO) unit content) for 30 mol% < $Li_2O \leq 40$ mol%, and a small decrease of the $BO_4$ content (together with a large increase of $BO_3$(NBO)) for $Li_2O$ > 40 mol% (§ 3.1). The way $E_a$ changes with composition can be tentatively discussed in the light of the structural evolution. For $Li_2O$ < 30 mol%, the large decrease of $E_a$ is related to the large increase of $Li^+$ associated with the formation of tetrahedrally coordinated boron units, $BO_4^-$, where $Li^+$ acts as a charge compensator and is weakly bonded. For 30 mol% < $Li_2O \leq$ 40 mol%, the decrease is less pronounced as both $BO_4$ and $BO_3$(NBO) form, resulting in stronger bonds with $Li^+$ ions, as reflected in the increase of the elastic moduli. The increase of $BO_3$(NBO) unit for $Li_2O$ > 40 mol% is associated with the formation of more strongly bonded $Li^+$ ions but, at the same time, the network becomes more open ($C_g$ goes down) and $Li^+$ ions have more room to travel through the network, by means of a hopping mechanism, so that $E_a$ keeps decreasing in this composition range. $E_a$ is close to 50 kJ mol$^{-1}$ at 50 mol% $Li_2O$, that is as the fraction of Li approaches 1 Li for 1 B/Al.

The molar volume (atom-gram) $V_0$ and $E_a$ are given as a function of the $Li_2O$ content in Fig. 8a. $V_0$, provides a measurement of the distance (~$V_0^{1/3}$) between two adjacent lithium sites. Therefore, the decrease of $E_a$ and the increase of $\sigma_i$ are associated with the decrease of the hopping distance ($l_0$) between two adjacent sites. In fact, $E_a$ is expressed as [42],

$$E_a = \frac{1}{2} m\, l_0^2\, v_0^2 \tag{19}$$

where $m$ is the molar mass of the mobile ion, and $v_0$ its vibrational frequency. The addition of $Al_2O_3$ into the LiB glasses increases $V_0$ as the bond length of Al-O (~1.87 Å) is longer than that of B-O (~1.28 Å) [44], but the incidence on $\sigma_i$ and $E_a$ remains limited (see Ref. [45] for details).

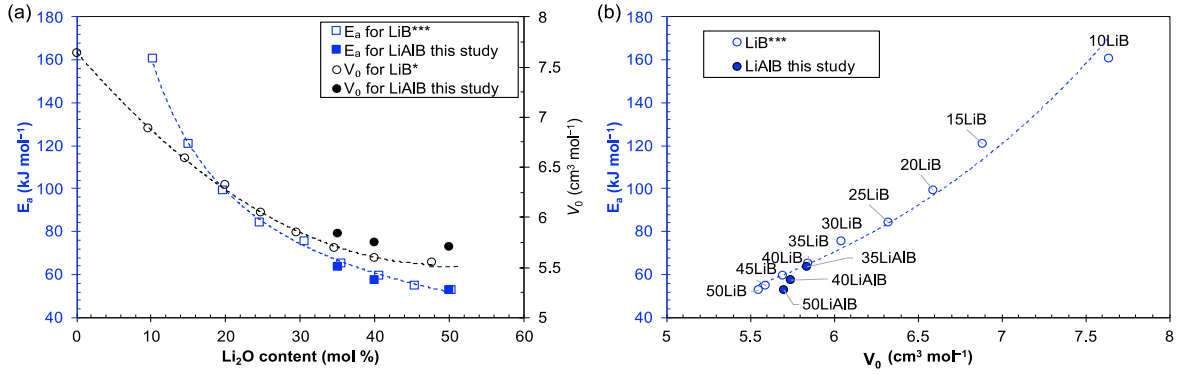


***Figure 8**. (a) Activation energy ($E_a$) of ionic conductivity and molar volume ($V_0$, as calculated with Eq. (2)) as a function of $Li_2O$ content. The experimental error on $V_0$ chiefly stems from the error on the glass density and is smaller than the points on the figure. ***Data extracted from Ref. [14]. *Data extracted from Ref. [37]. (b) $E_a$ as a function of $V_0$.*

### 3.4.2 Pressure dependence

In order to investigate the pressure dependence of the ionic conductivity, pellets from the 50LiAlB and 40LiAlB glasses were submitted to a compressive loading in-situ, during the conductivity measurement, and with a loading axis aligned with the one of the electric fields. The stress is increased from 0.2 to 0.97 MPa. The range of applied stress is comparable to the

stress needed to join the electrodes to the electrolyte in an all-solid-state battery [46]. For the electrochemical measurements, the set-up is the same as in § 3.4. The Nyquist diagrams obtained on the 50LiAlB under different compressive stress are shown in Figure 9a. An increase of the ionic resistance with the stress is observed. The corresponding ionic conductivities are shown in Figure 9b.

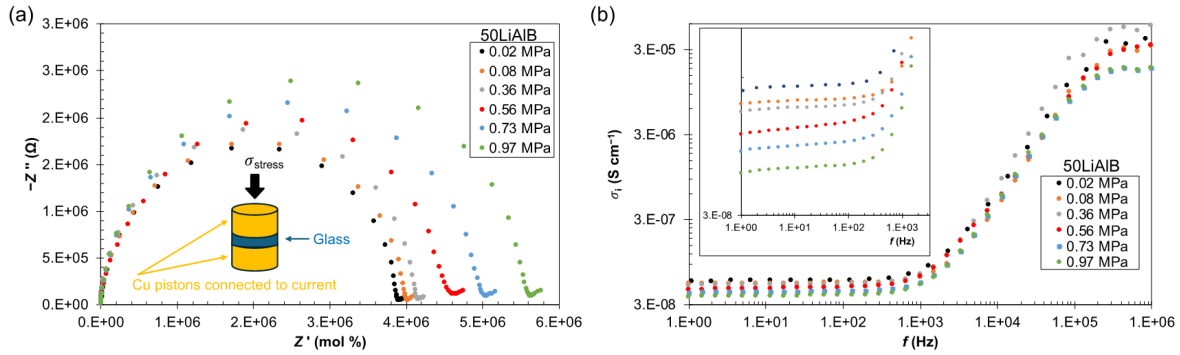


***Figure 9**. (a) Nyquist plot for the 50LiAlB glass under uniaxial compression. (b) Ionic conductivity spectra ($\sigma'_i$) for the 50LiAlB glass for different values of the stress.*

As diffusion is a pressure dependent thermally activated process, the ionic conductivity is associated with a free enthalpy of activation ($\Delta G_a$), referred to as the activation energy, and the corresponding activation volume expressed as,

$$\Delta V_a = \left(\frac{\partial \Delta G_a}{\partial p}\right)_{T,\ Structure} \tag{20}$$

where $p$ is the hydrostatic pressure ($p = -(1/3)\ \sigma_{stress}$, where $\sigma_{stress}$ is the applied stress (here, $\sigma_{stress} < 0$). The activation volume provides an estimation of the volume change occurring during the transport of the mobile ion, and with Eq. (14), on obtains,

$$\Delta V_a = RT\left[\frac{\partial \ln(\alpha_0)}{\partial p} - \frac{\partial \ln(T\sigma_i)}{\partial p}\right]_{T,\ Structure} \approx -RT\left[\frac{\partial \ln(T\sigma_i)}{\partial p}\right]_{T,\ Structure} \tag{21}$$

Here, $\alpha_0$ is assumed to change little with the stress, as the main stress effect is on the height of the energy barrier of the diffusion process [47]. The experimental determination of $\Delta V_a$ is illustrated in Figure 10.

Values of $\sigma_i$ measured below 0.2 MPa compressive stress are erroneous as they are associated with the establishment of the contact area between the copper contactors and the glassy electrolyte. At pressures above 0.2 MPa, points are nearly aligned with a straight line of negative slope, which allows to determine the activation volume, $V_a$. Activation volumes of 1.02 and 0.56 $cm^3 \cdot mol^{-1}$ are determined for the 50LiAlB and 40LiAlB glasses, respectively, using Eq. (20). Positive values of activation volumes reflect the fact that the glass structure needs to locally expand in order to allow the $Li^+$ ions migration between two adjacent "equilibrium" sites. Moreover, the larger activation volume of the 50LiAlB than that of the 40LiAlB suggests that the effect of pressure on the ionic conductivity is more pronounced for the 50LiAlB than for the 40LiAlB one. It turns out that the structures with more available volume per mobile ion ($V_{Li}$ in Table 1) exhibit smaller volume perturbation upon the diffusion process. However, additional investigations are clearly necessary to establish the link between the thermodynamic parameters of thermal activation of conductivity and the atomic structure of the glasses studied.

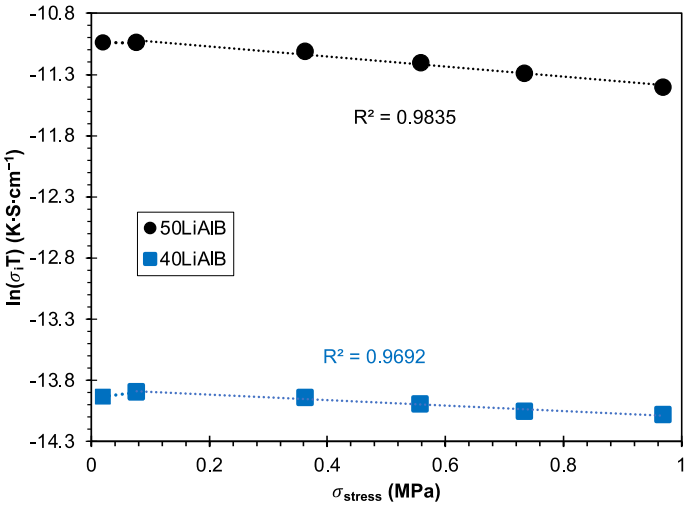


***Figure 10**. Ln($\sigma_i$T) as a function of applied $\sigma_{stress}$ for the 40LiAlB and 50LiAlB glasses. The first point is excluded from the analysis as it is associated with the setting of the contact between the electrolyte and the contactors.*

## 4. Conclusion

Young's and shear moduli, and hardness of glasses from the $Li_2O$-$B_2O_3$-$Al_2O_3$ system containing 35 to 50 mol.% $Li_2O$ decrease with increasing lithium content, while the ionic conductivity at 25 °C is increased from 3.7 $10^{-10}$ to 5.5 $10^{-8}$ S·cm$^{-1}$, and reaches about $10^{-5}$ S·cm$^{-1}$at 90 °C for the 50 % $Li_2O$. The indentation cracking resistance (*CR*) is also significantly reduced, from 1.7 to 0.5 N (at 50 % probability of cracking) as the $Li_2O$ content is increased from 35 to 50 mol.%. The superposition of a mechanical loading on the electric field (ionic conductivity measurement) reveals a mechano-electrical coupling. In the present case, $\sigma_i$ is found to decrease by about a factor 2 as the compressive stress is increased from zero to about 1 MPa. The dependence of $\sigma_i$ on the applied stress is reflected in the activation volume. The activation energy for the ionic conductivity decreases from about 65 to 55 kJ·mol$^{-1}$as the lithium content is increased, while the activation volume is raised from 0.56 to 1.02 cm$^3$·mol$^{-1}$. All these results were discussed in the light of the known structural changes, and in particular changes in the boron speciation, such as an increase of tetrahedrally coordinated boron for $Li_2O$ content up to 40 mol.%, and a steep increase of the amount of $BO_3$ triangular units with non-bridging oxygen at larger lithium concentration.

## Data availability statement

The data that support the findings of this study are available from the corresponding author upon reasonable request.

## Author contributions

**TT:** Conceptualization, Methodology, Investigation, Writing – Original Draft, Writing – Review & Editing; **IL:** Investigation, Formal analysis, Visualization; **PH:** Investigation, Visualization; **DLC:** Investigation, Formal analysis, Visualization; **LC:** Investigation, Formal analysis, Visualization; **AM:** Investigation, Formal analysis, Visualization; **SB:** Investigation, Formal analysis, Visualization; **MLF:** Investigation, Visualization; **TR:** Conceptualization, Methodology, Investigation, Writing – Review & Editing.

## Competing interests

The authors declare that they have no competing interests.

## Funding

This work was supported by the European Research Council through the ERC Advanced Grant (320506) and the European Union's Horizon 2020 research and innovation program under the Marie Skłodowska-Curie grant agreement (899546).

## Acknowledgement

We acknowledge Julien Chollet (Univ-Rennes) for his help in fabricating the machine for in-situ electrochemical measurement under compression.

## References

[1] J. B. Goodenough and Y. Kim, “Challenges for rechargeable Li batteries,” *Chem. Mater.*, vol. 22, no. 3, pp. 587–603, Feb. 2010, doi: 10.1021/cm901452z.

[2] J. Ding, D. Ji, Y. Yue, and M. M. Smedskjaer, “Amorphous materials for lithium-ion and post-lithium-ion batteries,” *Small*, vol. 20, no. 5, p. 2304270, 2024, doi: 10.1002/smll.202304270.

[3] L. Porz *et al.*, “Mechanism of lithium metal penetration through inorganic solid electrolytes,” *Adv. Energy Mater.*, vol. 7, no. 20, p. 1701003, 2017, doi: 10.1002/aenm.201701003.

[4] Z. Zhang *et al.*, “New horizons for inorganic solid state ion conductors,” *Energy Environ. Sci.*, vol. 11, no. 8, pp. 1945–1976, 2018, doi: 10.1039/c8ee01053f.

[5] T. Famprikis, P. Canepa, J. A. Dawson, M. S. Islam, and C. Masquelier, “Fundamentals of inorganic solid-state electrolytes for batteries,” *Nat. Mater.*, vol. 18, no. 12, pp. 1278–1291, 2019, doi: 10.1038/s41563-019-0431-3.

[6] A. Kato, M. Nose, M. Yamamoto, A. Sakuda, A. Hayashi, and M. Tatsumisago, “Mechanical properties of sulfide glasses in all-solid-state batteries,” *J. Ceram. Soc. Jpn.*, vol. 126, no. 9, 2018, doi: 10.2109/jcersj2.18022.

[7] Y. Daiko, A. Sakuda, T. Honma, and A. Hayashi, “Ionic conduction of glasses and their potential applications,” *J. Ceram. Soc. Jpn.*, vol. 130, no. 8, 2022, doi: 10.2109/jcersj2.22035.

[8] A. Pradel and M. Ribes, “Electrical properties of lithium conductive silicon sulfide glasses prepared by twin roller quenching,” *Solid State Ion.*, vol. 18–19, no. PART 1, 1986, doi: 10.1016/0167-2738(86)90139-6.

[9] Y. Seino, T. Ota, K. Takada, A. Hayashi, and M. Tatsumisago, “A sulphide lithium super ion conductor is superior to liquid ion conductors for use in rechargeable batteries,” *Energy Environ. Sci.*, vol. 7, no. 2, pp. 627–631, Jan. 2014, doi: 10.1039/C3EE41655K.

[10] K. E. Aifantis and J. P. Dempsey, “Stable crack growth in nanostructured Li-batteries,” *J. Power Sources*, vol. 143, no. 1–2, pp. 203–211, 2005, doi: 10.1016/j.jpowsour.2004.11.037.

[11] Z. Chen *et al.*, “Structure dependence of fracture toughness and ionic conductivity in lithium borophosphate glassy electrolytes for all-solid-state batteries,” *J. Power Sources*, vol. 553, p. 232302, 2023, doi: 10.1016/j.jpowsour.2022.232302.

[12] F. P. McGrogan *et al.*, “Compliant yet brittle mechanical behavior of $Li_2S$–$P_2S_5$ lithium-ion-conducting solid electrolyte,” *Adv. Energy Mater.*, vol. 7, no. 12, p. 1602011, Jun. 2017, doi: 10.1002/aenm.201602011.

[13] C. E. Athanasiou *et al.*, “Rate-dependent deformation of amorphous sulfide glass electrolytes for solid-state batteries,” *Cell Rep. Phys. Sci.*, vol. 3, no. 4, p. 100845, Apr. 2022, doi: 10.1016/j.xcrp.2022.100845.

[14] V. Montouillout *et al.*, “Ionic conductivity of lithium borate glasses and local structure probed by high resolution solid-sate NMR,” *J. Non-Cryst. Solids*, vol. 484, pp. 57–64, 2018, doi: 10.1016/j.jnoncrysol.2018.01.020.

[15] A. Levasseur and M. Menetrier, “Borate based lithium conducting glasses,” *Mater. Chem. Phys.*, vol. 23, no. 1–2, pp. 1–12, 1989, doi: 10.1016/0254-0584(89)90013-8.

[16] A. Ruckman *et al.*, “Lithium ion sites and their contribution to the ionic conductivity of $RLi_2O$-$B_2O_3$ glasses with R ≤ 1.85,” *Solid State Ion.*, vol. 359, p. 115530, 2021, doi: 10.1016/j.ssi.2020.115530.

[17] S. A. Feller, W. J. Dell, and P. J. Bray, “$^{10}$B NMR studies of lithium borate glasses,” *J. Non-Cryst. Solids*, vol. 51, no. 1, pp. 21–30, 1982, doi: 10.1016/0022-3093(82)90186-7.

[18] V. P. Klyuev and B. Z. Pevzner, “The influence of aluminum oxide on the thermal expansion, glass transition temperature, and viscosity of lithium and sodium aluminoborate glasses,” *Glass Phys. Chem.*, vol. 28, no. 4, pp. 207–220, 2002, doi: 10.1023/A:1019954010719.

[19] R. D. Shannon, “Revised effective ionic radii and systematic studies of interatomic distances in halides and chalcogenides,” *Acta Crystallogr. Sect. A*, vol. 32, no. 5, pp. 751–767, Sep. 1976, doi: 10.1107/S0567739476001551.

[20] J.-P. Poirier, *Introduction to the Physics of the Earth’s Interior*. Cambridge University Press, 2000.

[21] M. Sakai, “The Meyer hardness: A measure for plasticity?,” *J. Mater. Res.*, vol. 14, no. 9, pp. 3630–3639, Sep. 1999, doi: 10.1557/JMR.1999.0490.

[22] M. Wada, H. Furukawa, and K. Fujita, “Crack resistance of glass on Vickers indentation,” in *Proc. Int. Congr. Glass*, 1974, pp. 39–46.

[23] J. R. Macdonald, “Impedance spectroscopy,” *Ann. Biomed. Eng.*, vol. 20, pp. 289–305, 1992, doi: https://doi.org/10.1007/BF02368532.

[24] Y. C. Hu and H. Tanaka, “Origin of the boson peak in amorphous solids,” *Nat. Phys.*, vol. 18, no. 6, pp. 669–677, 2022, doi: 10.1038/s41567-022-01628-6.

[25] M. González-Jiménez *et al.*, “Understanding the emergence of the boson peak in molecular glasses,” *Nat. Commun.*, vol. 14, no. 1, p. 215, 2023, doi: 10.1038/s41467-023-35878-6.

[26] P. McMillan and B. Piriou, “Raman spectroscopy of calcium aluminate glasses and crystals,” *J. Non-Cryst. Solids*, vol. 55, no. 2, pp. 221–242, 1983, doi: 10.1016/0022-3093(83)90672-5.

[27] R. K. Brow, D. R. Tallant, and G. L. Turner, “Polyhedral arrangements in lanthanum aluminoborate glasses,” *J. Am. Ceram. Soc.*, vol. 80, no. 5, pp. 1239–1244, 1997, doi: 10.1111/j.1151-2916.1997.tb02970.x.

[28] W. L. Konijnendijk and J. M. Stevels, “The Structure of borate glasses studied by Raman scattering,” *J. Non-Cryst. Solids*, vol. 18, no. 3, pp. 307–331, 1975, doi: 10.1016/0022-3093(75)90137-4.

[29] A. K. Yadav and P. Singh, “A review of the structures of oxide glasses by Raman spectroscopy,” *RSC Adv.*, vol. 5, no. 83, 2015, doi: 10.1039/c5ra13043c.

[30] T. To, C. R. Pedersen, C. Gamst, M. H. Andersen, L. R. Jensen, and M. M. Smedskjaer, “Mechanical properties of hydrated cesium-lithium aluminoborate glasses,” *Phys. Rev. Mater.*, vol. 5, p. 83605, 2021, doi: 10.1103/PhysRevMaterials.5.083605.

[31] K. Januchta *et al.*, “Discovery of Ultra-Crack-Resistant Oxide Glasses with Adaptive Networks,” *Chem. Mater.*, vol. 29, no. 14, pp. 5865–5876, Jul. 2017, doi: 10.1021/acs.chemmater.7b00921.

[32] T. To *et al.*, “Comparing the effects of Ga2O3 and Al2O3 on the structure and mechanical properties of sodium borate glasses,” *J. Non-Cryst. Solids*, vol. 618, 2023, doi: 10.1016/j.jnoncrysol.2023.122506.

[33] T. Skopak *et al.*, “Mixture experimental design applied to gallium-rich $GaO_{3/2}$-$GeO_2$-$NaO_{1/2}$ glasses,” *J. Non-Cryst. Solids*, vol. 455, pp. 83–89, Jan. 2017, doi: 10.1016/J.JNONCRYSOL.2016.10.030.

[34] G. Padmaja and P. Kistaiah, “Infrared and raman spectroscopic studies on alkali borate glasses: Evidence of mixed alkali effect,” *J. Phys. Chem. A*, vol. 113, no. 11, pp. 2397–2404, Mar. 2009, doi: 10.1021/JP809318E/ASSET/IMAGES/JP-2008-09318E_M005.GIF.

[35] E. I. Kamitsos and G. D. Chryssikos, “Borate glass structure by Raman and infrared spectroscopies*,” *J. Mol. Struct.*, vol. 247, pp. 1–16, 1991.

[36] T. Rouxel, “What we can learn from crystals about the mechanical properties of glass,” *J. Ceram. Soc. Jpn.*, vol. 130, no. 8, pp. 519–530, 2022, doi: 10.2109/jcersj2.22067.

[37] S. S. Sørensen, H. Johra, J. C. Mauro, M. Bauchy, and M. M. Smedskjaer, “Boron anomaly in the thermal conductivity of lithium borate glasses,” *Phys. Rev. Mater.*, vol. 3, no. 7, p. 075601, 2019, doi: 10.1103/PhysRevMaterials.3.075601.

[38] T. Rouxel, “Elastic Properties and Short-to Medium-Range Order in Glasses,” *J. Am. Ceram. Soc.*, vol. 90, no. 10, pp. 3019–3039, Oct. 2007, doi: 10.1111/J.1551-2916.2007.01945.X.

[39] J. Gong, H. Miao, Z. Zhao, and Z. Guan, “Load-dependence of the measured hardness of Ti(C,N)-based cermets,” *Mater. Sci. Eng.*, vol. 303, no. 1–2, pp. 179–186, 2001, doi: 10.1016/S0921-5093(00)01845-1.

[40] O. Şahin, O. Uzun, U. Kölemen, and N. Uçar, “Dynamic hardness and reduced modulus determination on the (001) face of β-Sn single crystals by a depth sensing indentation technique,” *J. Phys. Condens. Matter*, vol. 19, no. 30, p. 17, Aug. 2007, doi: 10.1088/0953-8984/19/30/306001.

[41] C. Hays and E. G. Kendall, “An Analysis of Knoop Microhardness,” *METALLOGRAPHY*, vol. 6, no. 4, pp. 275–282, 1973, doi: 10.1016/0026-0800(73)90053-0.

[42] U. Strom and K. L. Ngai, “AC conductivity of Na-β$A\ell_2O_3$ from 102 Hz to 1011 Hz and from 0.02K to 600K: A generalized treatment,” *Solid State Ion.*, vol. 5, no. C, pp. 167–170, 1981, doi: 10.1016/0167-2738(81)90219-8.

[43] J. Newman and K. E. Thomas-Alyea, *Electrochemical systems*, 3rd edition. Wiley, Hoboken, NJ and Chichester, 2004.

[44] Y.-R. Luo and J.-P. Cheng, *Handbook of Chemistry and Physics*. Taylor & Francis.

[45] M. J. Rice and W. L. Roth, “Ionic transport in super ionic conductors: a theoretical model,” *J. Solid State Chem.*, vol. 4, no. 2, pp. 294–310, 1972, doi: 10.1016/0022-4596(72)90121-1.

[46] C. Fang *et al.*, “Pressure-tailored lithium deposition and dissolution in lithium metal batteries,” *Nat. Energy*, vol. 6, no. 10, pp. 987–994, 2021, doi: 10.1038/s41560-021-00917-3.

[47] J. J. Fontanella, “Pressure and temperature variation of the electrical conductivity of poly(propylene glycol) containing $LiCF_3SO_3$,” *J. Chem. Phys.*, vol. 111, no. 15, pp. 7103–7109, Oct. 1999, doi: 10.1063/1.480002.